

Fermi-surface topologies and low-temperature phases of the filled Skutterudite compounds $\text{CeOs}_4\text{Sb}_{12}$ and $\text{NdOs}_4\text{Sb}_{12}$

Pei Chun Ho^{1*}, John Singleton^{2,3†}, Paul A. Goddard⁴, Fedor F. Balakirev², Shalinee Chikara²,
Tatsuya Yanagisawa⁵, M. Brian Maple^{6,7}, David B. Shrekenhamer^{6†}, Xia Lee⁶ and Avraham T. Thomas^{6‡}

¹*Department of Physics, California State University, Fresno, CA 93740-8031, U.S.A.*

²*National High Magnetic Field Laboratory, Los Alamos National Laboratory, MS-E536, Los Alamos, NM 87545, U.S.A.*

³*University of Oxford, Department of Physics, The Clarendon Laboratory,*

Parks Road, Oxford, OX1 3PU, United Kingdom

⁴*Department of Physics, University of Warwick,*

Gibbet Hill Road, Coventry, CV4 7AL, United Kingdom

⁵*Department of Physics, Hokkaido University, Sapporo 060-0810, Japan*

⁶*Department of Physics, University of California, San Diego, La Jolla, CA 92093-0319, U.S.A.*

⁷*Center for Advanced Nanoscience, University of California, San Diego, La Jolla, CA 92093-0319, U.S.A.*

MHz conductivity, torque magnetometer and magnetization measurements are reported on single crystals of $\text{CeOs}_4\text{Sb}_{12}$ and $\text{NdOs}_4\text{Sb}_{12}$ using temperatures down to 0.5 K and magnetic fields of up to 60 tesla. The field-orientation dependence of the de Haas-van Alphen and Shubnikov-de Haas oscillations is deduced by rotating the samples about the [010] and [011] directions. The results indicate that $\text{NdOs}_4\text{Sb}_{12}$ has a similar Fermi surface topology to that of the unusual superconductor $\text{PrOs}_4\text{Sb}_{12}$, but with significantly smaller effective masses, supporting the importance of local phonon modes in contributing to the low-temperature heat capacity of $\text{NdOs}_4\text{Sb}_{12}$. By contrast, $\text{CeOs}_4\text{Sb}_{12}$ undergoes a field-induced transition from an unusual semimetal into a high-field, high-temperature state characterized by a single, almost spherical Fermi-surface section. The behavior of the phase boundary and comparisons with models of the bandstructure lead us to propose that the field-induced phase transition in $\text{CeOs}_4\text{Sb}_{12}$ is similar in origin to the well-known $\alpha - \gamma$ transition in Ce and its alloys.

I. INTRODUCTION

Filled skutterudite compounds, with the formula MT_4X_{12} , where M is an alkali metal, alkaline-earth, lanthanide, or actinide, T is Fe, Ru, or Os and X is P, As, or Sb, display a wide variety of interesting phenomena caused by strong electron correlations^{1–9}. Amongst these, the three compounds $\text{CeOs}_4\text{Sb}_{12}$, $\text{PrOs}_4\text{Sb}_{12}$, and $\text{NdOs}_4\text{Sb}_{12}$, formed by employing Periodic-Table neighbors for M, span the range from an antiferromagnetic (AFM) semimetal^{1,2} or perhaps Kondo insulator (M = Ce) [10] via a 1.85 K unconventional (quadrupolar-fluctuation mediated¹¹) superconductor (M = Pr) [8] to a 1 K ferromagnet (FM; M = Nd) [12]. In view of the low ordering temperatures, all around 1–2 K, associated with their various groundstates, plus precedents in other unconventional superconductors^{13,14}, it is tempting to speculate as to whether the superconductivity in M = Pr arises from close proximity to AFM and FM quantum-critical points, with the more explicitly magnetic M = Ce and M = Nd lying on the either side of the postulated quantum phase transitions. To explore this idea further, knowledge of the Fermi surfaces of all three materials is essential. Whilst the Fermi surface of $\text{PrOs}_4\text{Sb}_{12}$ is relatively well known⁸, those of $\text{CeOs}_4\text{Sb}_{12}$ and $\text{NdOs}_4\text{Sb}_{12}$ have been little studied. In this paper, we therefore use magnetic fields of up to 60 T to measure Fermi-surface cross-sections and effective masses for these two skutterudites. In the process we find a new magnetic-field-driven phase transition in $\text{CeOs}_4\text{Sb}_{12}$, whilst our measurements of $\text{NdOs}_4\text{Sb}_{12}$ point to the contribution of local phonon

modes to the low-temperature heat capacity.

The paper is organized as follows. Experimental details, including crystal growth and measurement techniques, are given in Section II. Sections III discusses high-field data from $\text{CeOs}_4\text{Sb}_{12}$, including evidence for the field-induced change in Fermi surface and the delineation of the new phase boundary at which this occurs, whilst the Fermi Surface of $\text{NdOs}_4\text{Sb}_{12}$ is treated in Section IV. Section V presents a summary and conclusions.

II. EXPERIMENTAL DETAILS

A. Crystal growth

Single crystals of $\text{CeOs}_4\text{Sb}_{12}$ and $\text{NdOs}_4\text{Sb}_{12}$ are synthesized using a molten-flux technique¹⁰ with an excess of Sb (40 to 1 ratio relative to the rare-earth element). The purities of the rare-earth elements are 3N; those of Os and Sb 4N and 5N respectively. Typical dimensions of the single crystals used in the experiments in this paper are $\sim 3.5 \times 0.4 \times 0.3 \text{ mm}^3$ for both compounds. The crystals have cubic space group $\text{Im}\bar{3}$; the cubic (non-primitive) unit cell and ion positions are shown in Figure 1(a). Further structural details are given in Refs. 15 and 16.

B. Quantum oscillation measurements

Both de Haas-van Alphen and Shubnikov-de Haas oscillations are used to determine the Fermi-surface cross-

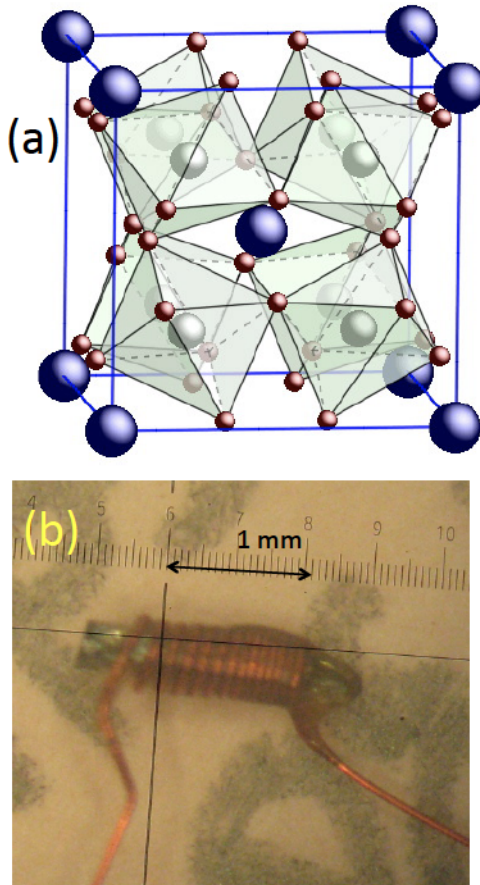


FIG. 1. (a) Cubic (non-primitive) unit cell for $\text{NdOs}_4\text{Sb}_{12}$ and $\text{CeOs}_4\text{Sb}_{12}$. Nd/Ce (corners and body center position) are purple; Os ions are gray, surrounded by cages with red Sb ions at the vertices. (b) Typical $\text{NdOs}_4\text{Sb}_{12}$ single crystal with proximity-detector oscillator coil (insulated 46 gauge, high-conductivity copper) wrapped around it.

sections of the two materials as a function of the orientation of the applied magnetic field. Oscillation frequencies and effective masses deduced from both techniques are found to be in good agreement. In addition, data taken using different crystals and batches of the same material are in accord within experimental errors, suggesting that the features described below are intrinsic to the two compounds.

Measurements of the de Haas-van Alphen effect are carried out in quasistatic magnetic fields and employ a torque magnetometer with a cantilever constructed from $5\ \mu\text{m}$ phosphor bronze³. A small slice taken from a single crystal is glued to the cantilever via a thin sheet of strain-reducing paper. The interaction between the sample's magnetic moment \mathbf{m} and the applied magnetic field \mathbf{B} causes a torque $-\mathbf{m} \times \mathbf{B}$ that results in a deflection of the cantilever. The deflection is monitored using the capacitance between the cantilever and a fixed plate about 1 mm below it ($\sim 0.5\ \text{pF}$), measured using a General Radio Capacitance bridge. Care is taken to ensure that deflections are small, so that the sample's orientation in the field is not changed significantly by the torque.

The torque magnetometer is mounted on a two-axis cryogenic goniometer that allows the sample orientation to be changed *in situ*; ^3He refrigeration provides temperatures in the range 0.45 – 10 K. Quasistatic magnetic fields are provided by a 35 T Bitter coil at NHMFL Tallahassee.

Shubnikov-de Haas oscillations are measured in pulsed magnetic fields using the contactless-conductivity method described in Refs. 17 and 18. A coil comprising 5 – 12 turns of 46-gauge high-conductivity copper wire is wound about the single-crystal sample (see Figure 1(b)); the number of turns employed depends on the cross-sectional area of the sample, with a larger number of turns being necessary for smaller samples. The coil forms part of a proximity detector oscillator (PDO) circuit resonating at 22-29 MHz. A change in the sample skin depth¹⁸ or differential susceptibility¹⁷ causes a change in the inductance of the coil, which in turn alters the resonant frequency of the circuit. Shubnikov-de Haas oscillations are observed in the resistivity and hence the skin depth and frequency^{17,18}. For the purposes of digitizing the data prior to Fourier transformation to obtain the frequency as a function of field, the signal from the PDO circuit is mixed down to about 2 MHz using a double heterodyne system^{17,18}. Data are recorded at 20 Msamples/s, well above the Nyquist limit. Two or three samples in individual coils coupled to independent PDOs are measured simultaneously, using a single-axis, worm-driven, cryogenic goniometer to adjust their orientation in the field. Pulsed magnetic fields are provided by the 60 T long-pulse magnet and one of the 65 T short-pulse magnets at NHMFL Los Alamos¹⁹; the former magnet, with its relatively slow rise time, is used to check that inductive sample heating is not an issue.

The goniometer is placed within a simple ^3He cryostat providing temperatures down to 0.4 K; temperatures are measured using a Cernox sensor supplied and calibrated by Lakeshore Inc. Magnetic fields are deduced by integrating the voltage induced in an eleven-turn coil, calibrated against the de Haas-van Alphen oscillations of the belly orbits of copper³. In both experiments, the crystals were either rotated about their [010] axis or their [110] axis, with the axis of rotation lying perpendicular to the magnetic field.

The phase boundary shown in Section III was traced using both the pulsed-field extraction magnetometer described in Ref. 20 and a commercial SQUID magnetometer (Quantum Design MPMS with 7 T magnet).

III. RESULTS ON CERIUM OSMIUM ANTIMONIDE

A. Overview of $\text{CeOs}_4\text{Sb}_{12}$ PDO data; phase boundary and quantum oscillations

Figure 2 shows the PDO frequency as a function of field for a variety of temperatures. As mentioned above, an increase in sample skin depth, due to an increase in

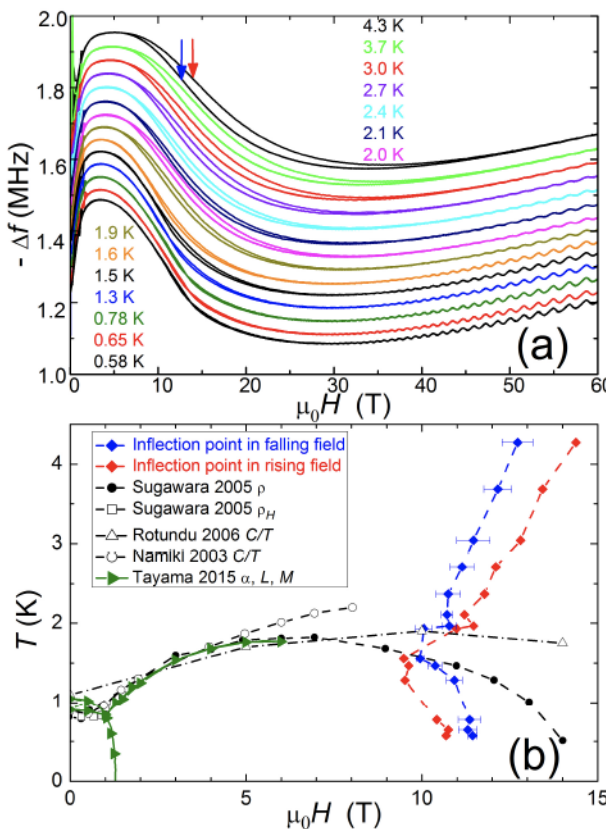


FIG. 2. (a) The negative of the PDO frequency shift, $-\Delta f$, observed for a CeOs₄Sb₁₂ single crystal plotted as a function of magnetic field for several sample temperatures T ; the color key for the various T is given within the figure. H is parallel to [100]. Data for both up- and down-sweeps of the field are shown; the blue (red) arrow indicates the position of the inflection point of the $-\Delta f$ versus H curve in falling (rising) field for the 4.3 K data set. Note Shubnikov-de Haas oscillations emerging at higher fields. (b) Inflection points in the $-\Delta f$ versus H curves shown in (a) plotted as a function of T . Notional phase boundaries supposedly enclosing the low-temperature antiferromagnetic state and deduced by other authors (Namiki *et al.* [22], Sugawara *et al.* [24], Rotundu *et al.* [21], Tayama *et al.* [1]) are shown for comparison; techniques and authors are shown in the inset key.

resistivity, will raise the inductance of the coil, as the sample excludes flux from a smaller area. Hence the PDO resonant frequency f will drop. For small changes it can be shown that¹⁷

$$\Delta f \propto -\Delta \rho \quad (1)$$

where Δf is the shift in frequency due to a change in sample resistivity $\Delta \rho$. Hence, Figure 2 has been plotted as $-\Delta f$ versus H , so that upward shifts in the data indicate increasing resistivity.

As the field increases, the resistivity rises steeply to a broad peak before falling to a minimum at about 25 T; note that within the region where the resistance falls there is hysteresis between the up- and downsweeps of the

magnetic field, suggestive of a phase boundary²³. From now on, we shall refer to the field regions on either side of this boundary as the L (low-field, low-temperature) and H (high-field, high-temperature) phases.

Following precedents set by similar, broad phase transitions²³, we plot the inflection point in the $-\Delta f$ versus H curves (see arrows in Fig. 2(a); in Fig. 2(b) in red (rising field) and blue (falling field). In previous work on CeOs₄Sb₁₂, a phase transition at $T \approx 1$ K with low entropy was detected; results from magnetoresistance, Hall effect, Sb nuclear quadrupole resonance (NQR), dilatometry and neutron-scattering experiments indicate that this low-temperature phase is intrinsic and originates from an antiferromagnetic (AFM) state, perhaps associated with a spin-density-wave (SDW) ground state.^{1,24–27} Notional phase boundaries enclosing this AFM state, deduced by other authors^{1,21,22,24} are shown in Figure 2(b) for comparison. The L to H transition marked by the fall in $-\Delta f$ around 11 T (red and blue points in Figure 2(b)) persists to temperatures well above the phase boundary around the antiferromagnetic state (black and hollow points). This shows that, above 2 K, the L to H transition cannot be *caused* by a field-induced destruction of the antiferromagnetic state (*c.f.* Ref. 28).

However, below 1.5 K and above 10 T, we believe that the L to H transition coincides with the boundary of the antiferromagnetic phase. In Section IIIC, we discuss changes in Fermi-surface topology and effective Ce valence that occur at the L to H transition; these are almost certain to destroy any antiferromagnetism. In this context, the features in the original data^{21,24} used by others to denote the high-field limit of the antiferromagnetic phase (Fig. 2(b), hollow triangles, black, filled circles); are rather broad. Given that the fall in $-\Delta f$ covers several tesla (Fig. 2(a)), we believe that the points measured below 1.5 K and between 10 and 15 T in Refs. 21 and 24 are in fact associated with the broadened L to H transition that we observe in the PDO data. Both of these collections of points lie within the extended field range of the fall in $-\Delta f$, and the scatter between the two data sets probably reflects the difficulty of assigning an exact field for such a broadened feature²³. The switching of the order of the up- and down-sweep L to H inflection points at low temperatures (Fig. 2(b), red and blue points) may well be a manifestation of the interdependence of the antiferromagnetic and L phases, a point to which we return in Section IIID.

At higher fields, (in the H phase), Shubnikov-de Haas oscillations can be seen superimposed on a gentle positive magnetoresistance (see Figures 2(a) and 3(a)). We shall now discuss these quantum oscillations, returning later to the origin of the L to H transition.

B. Shubnikov-de Haas oscillations and Fermi-surface topology in the H phase

A single frequency of Shubnikov-de Haas oscillations is observed in the H phase at all angles of the field; data such as those in Figure 3(b)) show that there is comparatively little angular variation of the extremal orbits, suggesting that the Fermi surface is likely to be an approximate sphere centred on the Γ point. The quasiparticle effective mass m^* was evaluated by examining the temperature (T) dependence of the Shubnikov-de Haas oscillation amplitude A (Figure 3(c)), and fitting it to the following portion of the Lifshitz-Kosevich formula²⁹:

$$\frac{A}{T} \propto \frac{1}{B \sinh(\frac{14.7T}{B} \frac{m^*}{m_e})}; \quad (2)$$

here, m_e is the mass of a free electron. A relatively light value of $m^*/m_e = 3.6 \pm 0.1$ was obtained for $\text{H}||[010]$.

The full angle dependence of the Shubnikov-de Haas oscillation frequency (and, via the Onsager relationship²⁹, the Fermi-surface cross-section) of CeSb₄Os₁₂ in the high-field phase is shown in Figure 4(a); for comparison, data for CeRu₄Sb₁₂ from Ref. 9 are also shown.

The low-temperature electrical resistivity of $\text{CeOs}_4\text{Sb}_{12}$ was initially interpreted in terms of a Kondo insulator with a small energy gap of ≈ 10 K [10]. However, bandstructure calculations^{2,30} suggest that $\text{CeOs}_4\text{Sb}_{12}$ is a compensated semimetal, with the chemical potential lying close to the bottom of an electron-like band (with very high density of states) and the top of a hole-like band, producing a Fermi surface consisting of tiny hole and electron pockets; this is shown schematically in Fig. 4(b). Yan *et al.* [2] remark that $\text{CeOs}_4\text{Sb}_{12}$ is very close to being a topological insulator². In the absence of symmetry breaking (for example caused by strain), the energy gap is zero, leading to the above-mentioned Fermi-surface pockets^{2,30}. The predicted Shubnikov-de Haas frequencies that would result from these calculated Fermi surfaces are much smaller than the experimental values shown in Fig. 4(a).

In Ref. 2, Yan *et al.* calculate the effect of removing electrons from the $\text{CeOs}_4\text{Sb}_{12}$ bandstructure; the result is a single, much larger, approximately spherical hole pocket centred on the Γ point (shown schematically in Fig. 4(c)). (The same conclusion can be derived from Fig. 3 of Ref. 30.) Such a Fermi-surface topology is qualitatively similar to our experimental observations in the H phase of $\text{CeOs}_4\text{Sb}_{12}$, providing, as we shall see in the following Section, a clue as to the cause of the L to H phase transition observed in Fig. 2.

C. Origin of the L to H phase boundary in CeOs₄Sb₁₂

Based on experimental evidence, we propose that the L to H phase transition in $\text{CeOs}_4\text{Sb}_{12}$ is a *valence transition*.

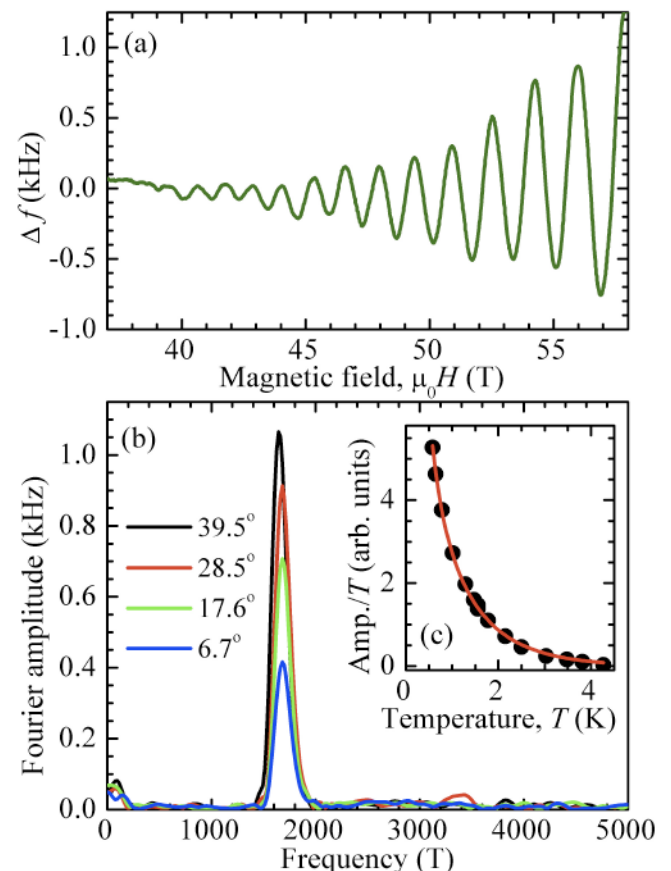


FIG. 3. (a) Shubnikov-de Haas oscillations in the PDO frequency shift of a CeOs₄Sb₁₂ single crystal, obtained by subtracting the monotonic background dependence due to magnetoresistance. The temperature is $T = 1.5$ K and the field is oriented at 28.5° to the [010] axis for rotation about the [110] axis. (b) Fourier transforms of data similar to those in (a) for the orientations shown in the inset key with respect to the [010] axis; $T = 1.5$ K and the sample is rotated about the [110] axis. (c) CeOs₄Sb₁₂ Shubnikov-de Haas-oscillation Fourier amplitude divided by T versus T ; data are points and the curve is a fit to Equation 2. H was applied parallel to the [001] direction.

tion^{23,31} analogous to those observed in YbInCu₄ [31–34], elemental Ce [31, 35–37] and Ce alloys such as Ce_{0.8}La_{0.1}Th_{0.1} [23]. In these materials, the valence transition occurs between a higher-temperature, higher-field phase in which quasi-localized 4f moments (on the Yb or Ce ions) are stabilized by entropy terms in the free energy, and a band-like state of the f electron at low temperatures and low fields³¹. For brevity, we refer to these phases as H and L respectively, just as in the case of CeOs₄Sb₁₂.

In the above materials, both the L and H phases are thought to possess correlated $4f$ electrons, but with very different effective Kondo temperatures^{23,31}. The effective Kondo temperatures of the H phases are small, so that the properties of the $4f$ electrons will be almost indis-

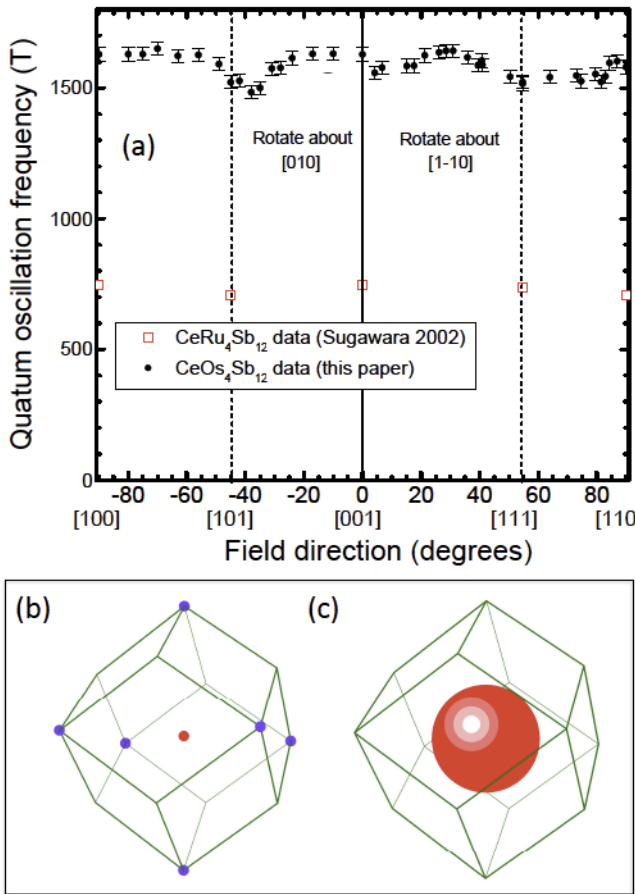


FIG. 4. (a) Field-orientation dependence of the Shubnikov-de Haas oscillation frequency of the H phase of $\text{CeOs}_4\text{Sb}_{12}$ (black points); For comparison, analogous data from $\text{CeRu}_4\text{Sb}_{12}$ taken from Ref. 9 are shown in red. (b) Schematic of semimetallic Fermi surface for $\text{CeOs}_4\text{Sb}_{12}$ and first Brillouin zone (dark green lines) based on Ref. 2. A tiny hole pocket at the zone-center Γ point (red) is compensated by electron pockets (purple) at the H points of the Brillouin zone; $\frac{1}{6}$ of each electron pocket is in the first Brillouin zone. (c) Schematic of $\text{CeOs}_4\text{Sb}_{12}$ Fermi surface after a downshift in chemical potential corresponding to the removal of itinerant quasiparticles from the bandstructure (based on Refs. 2 and 30). The discussion in Section IIIC suggests that the Fermi surface in the L phase is similar to that shown in (b), whilst the H-phase Fermi surface is similar to that shown in (c).

tinguishable from those of localized ionic moments^{23,31}; any remaining itinerant quasiparticles will have relatively light effective masses (as we observe experimentally in $\text{CeOs}_4\text{Sb}_{12}$; see the discussion of Fig. 3(c)). By contrast, the L phases of the above-mentioned systems have relatively large Kondo temperatures. This will cause the $4f$ electrons to be in the mixed-valence regime with significant spd and f hybridization, resulting in itinerant quasiparticles with a large effective mass^{23,31,32}. This is again in accord with the behavior of $\text{CeOs}_4\text{Sb}_{12}$; the L phase has an estimated Kondo temperature $T_{KL} \approx 100$ K [10], and evidence for a very heavy effective mass is given by

heat-capacity data^{10,21,22} that reveal a relatively large $\gamma = 92 - 180 \text{ mJmol}^{-1}\text{K}^{-2}$, despite the small itinerant carrier density³⁰.

In all such systems, the L-phase itinerant quasiparticles will be preferable to quasi-localized electrons from an energetic standpoint - they have smaller zero-point energy – at low temperatures, but quasi-localized $4f$ electrons will be favoured on entropic grounds at elevated temperatures³¹. Therefore, increasing the temperature will drive the L to H transition. Similarly, a magnetic field affects the free energy of the quasi-localized $4f$ electrons in the H phase more strongly than the energies of the band quasiparticles in either the L or H phases^{23,31}. Thus, the H phase becomes more energetically favorable with increasing field, so that a field-driven L to H transition occurs, as observed in $\text{CeOs}_4\text{Sb}_{12}$ and the other systems^{23,32-34}.

In common with our observations of $\text{CeOs}_4\text{Sb}_{12}$, the valence transitions from L to H phases in YbInCu_4 , Ce and Ce alloys are marked by (very frequently broadened) changes in resistivity and magnetic susceptibility, both accompanied by hysteresis in field and temperature sweeps^{23,32-37}. This type of transition is most spectacular in elemental Cerium and Ce alloys^{23,35-37}, where the L phase is known as the α phase, and H as the γ phase^{23,35-37}. Whereas the $4f$ ions in $\text{CeOs}_4\text{Sb}_{12}$ and YbInCu_4 represent a relatively small proportion of the elements in their respective solids, in Ce itself, *every* ion is involved, and the $\gamma - \alpha$ transition is accompanied by a 14.8% volume collapse as the redistribution of charge between ions and the sea of itinerant quasiparticles occurs; nevertheless, the face-centred-cubic (fcc) structure of Ce is preserved^{23,38}. This fascinating aspect of Cerium's behavior means that the $\gamma - \alpha$ transition has attracted considerable attention, especially in the metallurgy community (see Ref. 35 and references therein).

In the L phase of $\text{CeOs}_4\text{Sb}_{12}$, all of the available electrons will contribute to the sea of itinerant quasiparticles; $\text{CeOs}_4\text{Sb}_{12}$ will be a compensated semimetal^{2,30} with a Fermi surface similar to that shown schematically in Fig. 4(b). Though the carrier density is small, band-structure calculations³⁰ suggest that the chemical potential is located in a region where there exists a very large density of states associated with bands derived mostly from the $4f$ orbitals, leading to a large electronic heat capacity^{10,21,22}. On moving from the L to the H phase, the removal of f electrons from the itinerant quasiparticle sea will have the effect of lowering the chemical potential, leading to a hole Fermi surface at the Γ point, similar to that shown in Fig. 4(c) [2]. In $\text{CeOs}_4\text{Sb}_{12}$, the transition from a small density of very heavy quasiparticles (L phase) to a larger Fermi surface of much lighter holes (H phase) should lower the resistivity, as is indeed observed experimentally (Fig. 2(a)); this is in contrast to the case of Ce, where the very different bandstructure leads to a rise in resistance on going from α (L) to γ (H) [23]. Finally, as the chemical potential in $\text{CeOs}_4\text{Sb}_{12}$ moves down at the L to H transition, away from the bands with

the high density of states³⁰, the electronic contribution to the heat capacity should also fall, despite the larger Fermi surface^{30,40}; experiments carried out at fields close to the L to H border seem to suggest that γ indeed falls with increasing field²¹.

The antiferromagnetic state of $\text{CeOs}_4\text{Sb}_{12}$ has been attributed to a possible SDW state^{1,24–27}. SDWs are usually associated with features of the Fermi-surface topology⁴¹; therefore, as the Fermi surface changes as one crosses from L to the H phase, one would expect the antiferromagnetic state to be destroyed, as we argued in the discussion of Fig. 2 above.

D. Delineating the L to H phase boundary in $\text{CeOs}_4\text{Sb}_{12}$

Section II described how the PDO response is a convolution of the electrical resistance *and* the (magnetic) differential susceptibility¹⁷; in the phase-transition mechanism described above, both of these quantities are expected to change at the L to H boundary, with unpredictable consequences for the PDO frequency⁴². We therefore attempt a better delineation of the L to H phase boundary using magnetometry. Fig. 5(a) shows a pulsed-field measurement of the magnetization $M(H)$ at a temperature of 0.58 K. A change in the behavior of $M(H)$ occurs at a field close to the shift in PDO frequency that we associate with the L to H transition (Fig. 2); at high fields the differential susceptibility dM/dH is relatively small, whereas at lower fields it is larger and varies rapidly, leading to a curved $M(H)$ trace. The fine black line in Fig. 5(a) is provided as a guide to the eye in distinguishing the two regimes. Note that the α (L) to γ (H) transition in Ce alloys is also accompanied by an analogous, fairly gradual, change in dM/dH [23].

Free-energy considerations³¹ show that increases in temperature also favor quasi-localized $4f$ electrons; therefore, increasing temperature should drive the system through the L to H transition at zero magnetic field. Fig. 5(b) shows zero-field temperature-dependent resistivity ($\rho(T)$) data for two of the $\text{CeOs}_4\text{Sb}_{12}$ samples used in this study; a distinct minimum is seen close to $T = 15$ K. The L phase, with its small number of heavy quasiparticles, will have a high ρ at low temperatures, whereas the H phase, with its simpler, larger Fermi surface of lighter quasiparticles, should exhibit relatively conventional metallic $\rho(T)$ behavior at higher temperatures; therefore, we associate the minimum in $\rho(T)$ with the boundary between these two regimes.

Fig. 5(c) is a compilation of the various data in an attempt to identify the complete L to H phase boundary. The color scale and contours are differential susceptibility (dM/dH) data derived by differentiating $M(H)$ curves such as that in Fig. 5(a); the whole plot is an interpolation of data from 20 T pulsed-field sweeps at temperatures of 0.58, 1.33, 2.54, 3.12, 3.64, 4.30, 5.00, 5.50, 6.00, 6.50, 7.00, 7.50, 8.50, 9.00, 10.00, 11.00, 13.50,

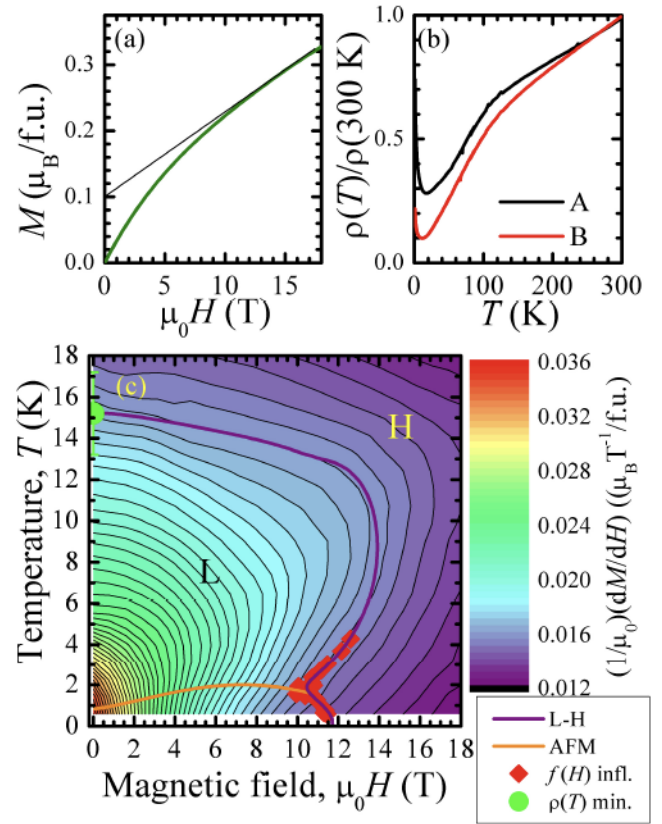


FIG. 5. (a) Pulsed-field measurement of the magnetization $M(H)$ of a $\text{CeOs}_4\text{Sb}_{12}$ crystal for $H||c$ and $T = 0.58$ K. The units of $M(H)$ are μ_B per formula unit (f.u.). Data are shown in dark green; the fine line is shown as a guide to the eye, indicating the rapidly increasing magnitude of dM/dH as the field falls below about 11 T. (b) Resistivity $\rho(T)$ normalized to the value at 300 K versus temperature for two crystals (A, B) of $\text{CeOs}_4\text{Sb}_{12}$. A minimum around $T \approx 15$ K is clearly visible. (c) Phase diagram of $\text{CeOs}_4\text{Sb}_{12}$ including a contour plot of dM/dH versus field $\mu_0 H$ and temperature T . The green point is the average position of the minimum in resistance (see (b)) for our samples, with the error bar showing the spread of values; red points are the falling-field inflection points from the PDO data (see Fig. 2). The orange curve is the boundary of the antiferromagnetic state, derived by averaging the points of various authors shown in Fig. 2(b), but truncated by the L to H transition at high fields. The purple curve is the notional phase boundary between the H and L phases.

15.00, 16.00 and 18.00 K, plus constant-field temperature sweeps (40–2 K) in the SQUID at fields of 0.1, 0.5, 1, 2, 3, 4, 5, 6 and 7 T. The resistivity minimum (Fig. 5(b)) and the features from the low-temperature PDO data (Fig. 2) are superimposed on the plot, along with the boundary around the antiferromagnetic phase (orange curve).

As discussed above, the L phase seems to be characterized by a relatively high dM/dH , and the H phase by lower, less field-dependent values. At temperatures above 1.5 K, our notional boundary between L and H phases is therefore based on the idea that some char-

acteristic value of the differential susceptibility (*i.e.* a contour in Fig. 5(c)) separates the two states³⁹. To this end, note that the resistive minimum and the kinks in the PDO data above 1.5 K lie at very similar values of dM/dH . We therefore trace a notional L to H phase boundary that connects these points, roughly following the dM/dH contours (Fig. 5(c); purple curve).

Sections IIIA and IIIC describe how, below 1.5 K and above 10 T, we expect the L to H transition and the boundary of the antiferromagnetic phase to coincide; below 1.5 K, the notional phase boundary follows the PDO data to reflect the change in character of the L to H transition observed in this region (see Fig. 2).

At first sight, by analogy with other correlated-electron systems^{13,14,45}, it is tempting to ascribe the antiferromagnetic phase to a region of quantum fluctuations around some point at which the L to H transition plunges to $T = 0$. However, the susceptibility contours (and, presumably, the L to H phase boundary) are unusual in curving back towards the origin at low temperatures. Related behavior has been seen in the phase diagrams of reduced-dimensionality antiferromagnets^{43,44}; but by contrast, in those cases, the effect occurred on the high- T , low- H side of the phase boundary and was attributed to the effect of thermal fluctuations on the free energy of the system⁴³. In the case of $\text{CeOs}_4\text{Sb}_{12}$, the reverse curvature instead occurs close to the low-temperature antiferromagnetic state (orange phase boundary in Fig. 5(c)); it is possible that the effect is due here to antiferromagnetic quantum fluctuations, rather than thermal fluctuations.

In summary, the L to H transition in $\text{CeOs}_4\text{Sb}_{12}$ behaves in many ways (*i.e.* broadness, hysteresis, gentle changes in resistivity and differential susceptibility) very similarly to the $\alpha - \gamma$ (L-H) transition observed in Ce and its alloys^{23,31}. The apparent change in Fermi surface from the compensated semimetal predicted by bandstructure calculations (L phase) to the single, approximately spherical, much larger pocket evidenced by the quantum oscillations in the H phase is also in accord with such an explanation. In effect, some of the charge carriers undergo a transition from delocalized quasiparticles (L phase) to localized Ce 4f electrons (H phase)⁴⁶.

IV. NEODYMIUM OSMIUM ANTIMONIDE

Figure 6(a) shows typical quantum-oscillation data for $\text{NdOs}_4\text{Sb}_{12}$; a Fourier transform is given in Figure 6(b). Depending on the orientation of the magnetic field, as many as five separate frequencies may be visible, or as few as two. One of the frequencies observed was very obviously a second harmonic, suggestive of well-resolved spin splitting of the fundamental frequency²⁹.

The frequencies observed in $\text{NdOs}_4\text{Sb}_{12}$ are plotted in Figure 7 as a function of the orientation of the magnetic field. For comparison, frequencies measured in de Haas-van Alphen experiments on $\text{PrOs}_4\text{Sb}_{12}$ reported in Ref. 8 are shown as continuous curves; for convenience, we use

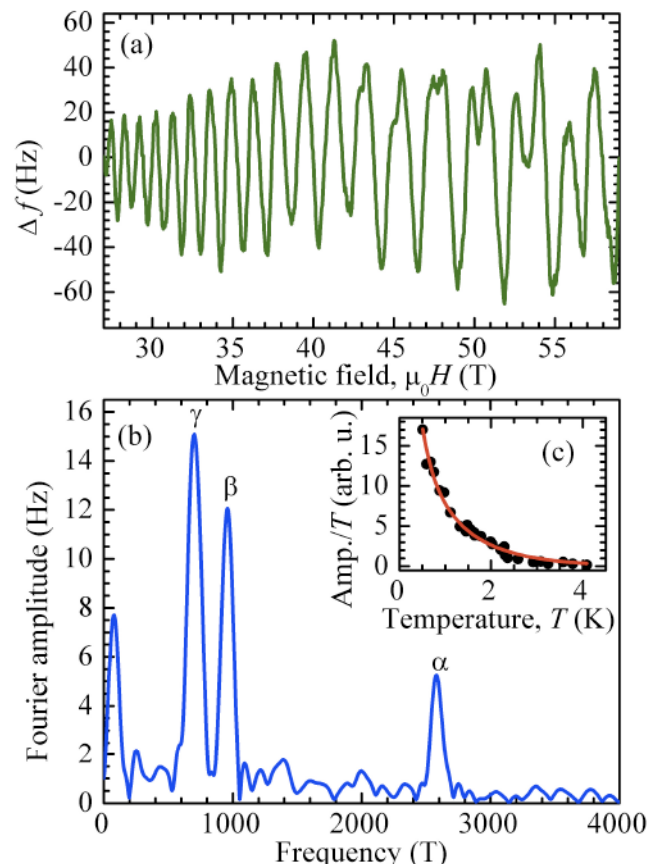


FIG. 6. (a) Shubnikov-de Haas oscillations in the PDO frequency shift of a $\text{NdOs}_4\text{Sb}_{12}$ single crystal, obtained by subtracting the monotonic background dependence due to magnetoresistance. The temperature is $T = 1.5$ K and the field is oriented at 39.5° to the $[0\bar{1}0]$ axis for rotation about the $[1\bar{1}0]$ axis. (b) Fourier transforms of data similar to those in (a) for H making an angle of 6.7° with respect to the $[0\bar{1}0]$ axis; $T = 1.5$ K and the sample is rotated about the $[1\bar{1}0]$ axis. The peak close to 90 T is thought to be an artefact of the background subtraction routine. The Fermi-surface sections are labelled α , β and γ following the scheme used in $\text{PrOs}_4\text{Sb}_{12}$ [8]. (c) $\text{NdOs}_4\text{Sb}_{12}$ α -frequency Shubnikov-de Haas oscillation Fourier amplitude divided by T versus T ; data are points and the curve is a fit to Equation 2. H was applied parallel to the $[001]$ direction.

the same cross-section labels as that work. Overall, the Fermi-surface topologies of the two materials are similar, with the β Fermi-surface section being slightly smaller in $\text{NdOs}_4\text{Sb}_{12}$ than in the Pr-compound. The α sheet of the two materials is also similar, with that in $\text{NdOs}_4\text{Sb}_{12}$ being somewhat slimmer for fields close to the $[101]$ directions. By contrast, the γ sheet is somewhat larger in $\text{NdOs}_4\text{Sb}_{12}$.

A single, higher frequency around 3800 T was observed for fields close to alignment with $[101]$; though an equivalent is not seen in experimental data for $\text{PrOs}_4\text{Sb}_{12}$, it is very similar to one of the frequencies predicted from that material's bandstructure calculations⁸. For this particu-

Field orientation	Fermi-surface section	NdOs ₄ Sb ₁₂ (this paper)		PrOs ₄ Sb ₁₂ (Ref. 8)	
		<i>F</i> (T)	<i>m</i> [*] / <i>m</i> _e	<i>F</i> (T)	<i>m</i> [*] / <i>m</i> _e
$\mathbf{H} \parallel [001]$	α	2560 ± 20	3.1 ± 0.2	2610	4.1
$\mathbf{H} \parallel [001]$	β	950 ± 20	1.8 ± 0.3	1070	2.5
$\mathbf{H} \parallel [001]$	γ	690 ± 30	3.6 ± 0.4	710	7.6
$\mathbf{H} \parallel [011]$	β	870 ± 30	1.5 ± 0.4	875	3.9

TABLE I. Effective masses and quantum-oscillation frequencies for NdOs₄Sb₁₂ and PrOs₄Sb₁₂.

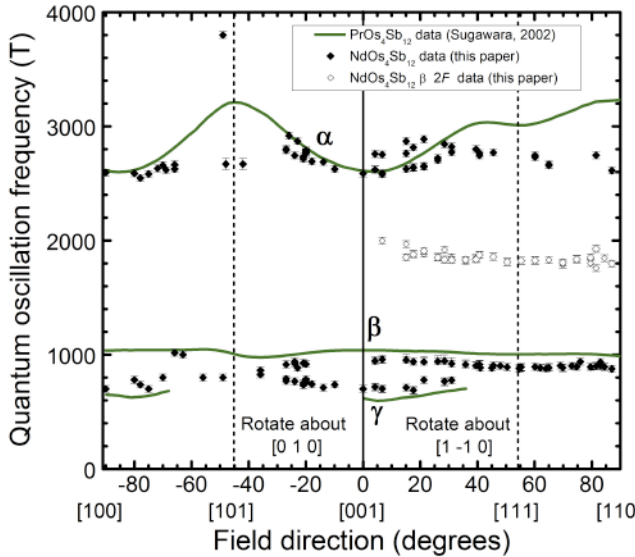


FIG. 7. Quantum-oscillation frequencies versus field orientation for NdOs₄Sb₁₂; points correspond to well-resolved frequencies observed in the data; the curves are analogous data from PrOs₄Sb₁₂ taken from Reference 8. The Fermi-surface sections are labelled according to the scheme used in the latter reference for PrOs₄Sb₁₂.

lar Fermi-surface section⁸, when $\mathbf{H} \parallel [101]$, it appears that the Fermi surface cross-sectional area changes relatively slowly as one moves away from the extremal orbit along a direction $\mathbf{k} \parallel \mathbf{H}$. Such a topology will give an enhanced quantum-oscillation amplitude for a narrow range of angles around this field orientation²⁹. Moreover, as discussed below, the effective masses are generally lower in NdOs₄Sb₁₂ than in PrOs₄Sb₁₂, favoring the observation of quantum oscillations in the former.

Band structure calculations for PrOs₄Sb₁₂ predict a splitting of the α frequency for fields around the [001] direction; this was not observed in PrOs₄Sb₁₂ [8] but seems to be resolved in the present experiments on NdOs₄Sb₁₂.

Effective masses m^* were derived from the temperature dependence of the oscillation amplitudes as shown in Figure 6(c); values are tabulated in Table I, and analogous data for PrOs₄Sb₁₂ are shown for comparison. The masses for NdOs₄Sb₁₂ are consistently smaller than their equivalents in PrOs₄Sb₁₂, suggesting that the interactions that lead to mass renormalization are smaller in

the former compound.

As mentioned in the Introduction, NdOs₄Sb₁₂ is a ferromagnet with an ordering temperature $T_C \approx 1$ K displaying mean-field ferromagnetism¹². Its temperature-linear heat-capacity coefficient is $\gamma \approx 520 \text{ mJmol}^{-1}\text{K}^{-2}$; that for PrOs₄Sb₁₂ is $\gamma \approx 650 \text{ mJmol}^{-1}\text{K}^{-2}$ [8]. The fact that the effective masses are significantly larger in the latter than the former (Table I), whilst the γ values are relatively close, suggests that another contribution to γ might be present in NdOs₂Sb₁₂. Theoretical models indicate that the off-center potential minima of the six rare earth sites (see Figure 1(a)) could give rise to local phonons and enhance the electron-phonon interaction in the filled skutterudites.^{48–50} This effect results in Kondo-like phenomena, but with a non-magnetic origin; it can also contribute to a large electronic γ . These models have been used to explain the large magnetic-field-independent $\gamma \approx 820 \text{ mJmol}^{-1}\text{K}^{-2}$ in SmOs₄Sb₁₂.^{51,52} Previous ultrasonic measurements show an extra mode in NdOs₄Sb₁₂ at $T \approx 15$ K [53–55]; it and the above-mentioned SmOs₄Sb₁₂ are the only two skutterudites displaying this ultrasonic anomaly^{53–55}. The contrast between the relatively low cyclotron effective masses in NdOs₄Sb₁₂ and its relatively high γ value is therefore probably due to the local phonon modes.

V. CONCLUSIONS

Magnetometry and high-frequency conductivity measurements have been made on single crystals of CeOs₄Sb₁₂ and NdOs₄Sb₁₂ using temperatures down to 0.5 K and magnetic fields of up to 60 tesla. The data show that CeOs₄Sb₁₂ undergoes a field-induced transition from a semimetal L phase into a high-field, high-temperature H phase characterized by a single, almost spherical Fermi-surface section. The general behaviour of the phase transition and comparisons with models of the bandstructure lead us to propose that the field-induced phase transition in CeOs₄Sb₁₂ is similar in origin to the well-known $\alpha - \gamma$ transition in Ce and its alloys²³. The phase boundary appears to exhibit an unusual curvature at low temperatures, possibly due to quantum fluctuations associated with the antiferromagnetic phase. By contrast, the behavior of NdOs₄Sb₁₂ is relatively straightforward; it has a similar Fermi surface topology to that of PrOs₄Sb₁₂, but with significantly

smaller effective masses. This result supports the importance of local phonon modes in contributing to the low-temperature heat capacity of $\text{NdOs}_4\text{Sb}_{12}$. The original motivation for this study – to investigate whether the superconductivity in $\text{PrOs}_4\text{Sb}_{12}$ arises from close proximity to AFM and FM quantum-critical points, with the more explicitly magnetic $\text{CeOs}_4\text{Sb}_{12}$ and $\text{NdOs}_4\text{Sb}_{12}$ lying on the either side of the postulated quantum phase transitions – is borne out in part. $\text{NdOs}_4\text{Sb}_{12}$ and $\text{PrOs}_4\text{Sb}_{12}$ indeed look like close relatives, with the heavier quasiparticle masses in the latter favoring superconductivity. But any resemblance of $\text{CeOs}_4\text{Sb}_{12}$ to the other two Skutterudites is overwhelmed by the Kondo physics that is often writ large in Ce and its compounds.

VI. ACKNOWLEDGMENTS

Research at CSU-Fresno is supported by NSF DMR-1506677. Work at UCSD is supported by the US Department of Energy, Office of Basic Energy Sciences, Division of Materials Sciences and Engineering, under Grant No. DEFG02-04ER46105 (single crystal growth) and the National Science Foundation under Grant No.

DMR 1206553 (sample characterization). The portion of this work done at Hokkaido University is supported by JSPS KAKENHI grants nos. 26400342, 15K05882 and 15K21732. Research at the University of Warwick is supported by EPSRC. A portion of this work was performed at the National High Magnetic Field Laboratory, which is supported by National Science Foundation Cooperative Agreement No. DMR- 1157490, the State of Florida, and the U.S. Department of Energy (DoE) and through the DoE Basic Energy Science Field Work Proposal “Science in 100 T”. JS thanks the University of Oxford for provision of a visiting professorship that permitted the low-field measurements featured in this paper. We are very grateful to H. Harima for many illuminating comments on an earlier version of this manuscript.

*Contact email pcho@csufresno.edu

†Contact email jsingle@lanl.gov

‡Current address: Johns Hopkins University Applied Physics Laboratory, 11100 Johns Hopkins Road, Laurel MD 20723, U.S.A.

§Current address: Lawrence Livermore National Laboratory, P.O. Box 808, Livermore, CA 94551-0808.

¹ T. Tayama, W. Ohmachi, M. Wansawa, D. Yutani, T. Sakakibara, H. Sugawara and H. Sato, *J. Phys. Soc. Jpn.* **84**, 104701 (2015).

² Binghai Yan, Lukas Mühler, Xiao-Liang Qi, Shou-Cheng Zhang and Claudia Felser *Phys. Rev. B* **85**, 165125 (2012).

³ Pei-Chun Ho, J. Singleton, M.B. Maple, Hisatomo Harima, P.A. Goddard, Z. Henkie and A Pietraszko, *New J. Phys.* **9**, 269 (2007).

⁴ Y. Aoki, H. Sugawara, H. Harima, and H. Sato, *J. Phys. Soc. Jpn.* **74**, 209 (2005).

⁵ M.B. Maple, E.D. Bauer, N.A. Frederick, P.-C. Ho, W.A. Yuhasz, and V.S. Zapf, *Physica B* **328**, 28 (2003).

⁶ G.P Meisner, M.S. Torikachvili, K.N. Yang, M.B. Maple and R.P. Guertin, *J. Appl. Phys.* **57**, 3073 (1985).

⁷ H. Sugawara, T.D. Matusda, K. Abe, Y. Aoki, H. Sato, S. Nojiri, Y. Inada, R. Settai and Y. Onuki, *Phys. Rev. B* **66**, 134411 (2002).

⁸ H. Sugawara, S. Osaki, S.R. Saba, Y. Aoki, H. Sato, Y. Inada, H. Shishido, R. Settai, Y. Onuki, H. Harima and K. Oikawa, *Phys. Rev. B* **66**, 220504(R) (2002).

⁹ H. Sugawara, K. Abe, T.D. Matsuda, Y. Aoki, H. Sato, R. Settai and Y. Onuki, *Physica B* **312-313**, 264 (2002).

¹⁰ E. D. Bauer, A. Ślebarski, E. J. Freeman, C. Sirvent, and M. B. Maple, *J. Phys.: Condens. Matter* **13**, 4495 (2001).

¹¹ K. Miyake, H. Kohno and H. Harima, *J. Phys.: Condens. Matter* **15**, L275 (2003).

¹² P.-C. Ho, W. M. Yuhasz, N. P. Butch, N. A. Frederick, T. A. Sayles, J. R. Jeffries, M. B. Maple, J. B. Betts, A. H. Lacerda, P. Rogl, and G. Giester, *Phys. Rev. B* **72**, 094410 (2005).

¹³ John S. Van Dyke, Freeke Massee, Milan P. Allan, J.C. Seamus Davies, Cedomir Petrovic and Dirk K. Morr, *PNAS* **111**, 11663 (2014), and references therein.

¹⁴ Jaime Merino and Ross H. McKenzie, *Phys. Rev. Lett.* **87**, 237002 (2001).

¹⁵ M.B. Maple, N.P. Butch, N.A. Frederick, P.-C. Ho, J.R. Jeffries, T.A. Sayles, T. Yanagisawa, W.M. Yuhasz, Songxue Chi, H.J. Kang, J.W. Lynn, Pengcheng Dai, S.K. McCall, M.W. McElfresh, M.J. Fluss, Z. Henkie and A. Pietraszko, *PNAS* **103**, 6783 (2006).

¹⁶ W.M. Yuhasz, N.P. Butch, T.A. Sayles, P.-C. Ho, J.R. Jeffries, T. Yanagisawa, N.A. Frederick, M.B. Maple, Z. Henkie, A. Pietraszko, S.K. McCall, M.W. Mc Elfresh and M.J. Fluss, *Phys. Rev. B* **73**, 144409 (2006).

¹⁷ S. Ghannadzadeh, M. Coak, I. Franke, P. A. Goddard, J. Singleton and J. L. Manson *Rev. Sci. Instrum.* **82**, 113902 (2011).

¹⁸ M.M. Altarawneh, C.H. Mielke and J.S. Brooks, *Rev Sci Instrum.* **80**, 066104 (2009).

¹⁹ J. Singleton, C.H. Mielke, A. Migliori, G.S. Boebinger and A.H. Lacerda, *Physica B* **346**, 614 (2004) and references therein.

²⁰ P. Goddard, J. Singleton, P. Sengupta, R. D. McDonald, T. Lancaster, S. J. Blundell, F. L. Pratt, S. Cox, N. Harrison, J. L. Manson, H. I. Southerland, and J. A. Schlueter, *New J. Phys.* **10**, 083025 (2008).

²¹ C.Rotundu and B. Andraka, *Phys. Rev. B* **73**, 144429 (2006).

²² T. Namiki, Y. Aoki, H. Sugawara, and H. Sato, *Acta. Phys. Polonica B* **34**, 1161 (2003).

²³ F. Drymiotis, J. Singleton, N. Harrison, L. Balicas, A. Bangura, C.H. Mielke, Z. Fisk, A. Migliori, J.L. Smith and J.C. Lashley, *J.Phys.: Condens. Matter* **17**, L77 (2005).

²⁴ H. Sugawara, S. Osaki, M. Kobayashi, T. Namiki, S. R. Saha, Y. Aoki, and H. Sato, *Phys. Rev. B* **71**, 125127 (2005).

²⁵ M. Yogi, H. Kotegawa, G. Q. Zheng, Y. Kitaoka, S. Ohsaki, H. Sugawara, and H. Sato, *J. Phys. Soc. Jpn.* **74**, 1950 (2005).

²⁶ C. Yang, Z. Zhou, H. Wang, J. Hu, K. Iwasa, H. Sugawara, and H. Sato, *Rare Metals* **25**, 550 (2006).

²⁷ C. P. Yang, H. Wang, J. F. Hu, K. Iwasa, K. Kohgi, H. Sugawara, and H. Sato, *J. Phys. Chem. C* **111**, 2391 (2007).

²⁸ N. Harrison, S.E. Sebastian, C.H. Mielke, A. Paris, M.J. Gordon C.A. Swenson, D.G. Rickel, M.D. Pacheco, P.F. Ruminer, J.B. Schillig, J.R. Sims, A.H. Lacerda, M.-T. Suzuki, H. Harima and T. Ebihara, *Phys. Rev. Lett.* **99**, 056401 (2007).

²⁹ D. Shoenberg, *Magnetic oscillations in metals*, Cambridge University Press (Cambridge, 1984).

³⁰ H. Harima and K. Takegahara, *J. Phys.: Condensed Matter* **15**, S2081 (2003).

³¹ M.O. Dzero, L.P. Gorkov and A.K. Zvezdin, *J. Phys.: Condens. Matter* **12**, L711 (2000).

³² J.L. Sarrao, A.P. Ramirez, T.W. Darling, F. Freibert, A. Migliori, C.D. Immer, Z. Fisk and Y. Uwatoko, *Phys. Rev. B* **58**, 409 (1998).

³³ C.D. Immer, J.L. Sarrao, Z. Fisk, A. Lacerda, C. Mielke and J.D. Thompson, *Phys. Rev. B* **56**, 71 (1997).

³⁴ J.L. Sarrao, *Physica B* **259-261**, 128 (1999).

³⁵ D.C. Koskenmaki and K.A. Gschneider, p337, *Handbook on the Physics and Chemistry of Rare Earths*, ed. K.A. Gschneider and L. Eyring (North Holland, Amsterdam, 1978).

³⁶ J. Laegsgaard and A. Svane, *Phys. Rev. B* **59**, 3450 (1999).

³⁷ K. Held, A.K. McMahan and R.T. Scaletter, *Phys. Rev. Lett.* **87**, 276404 (2001).

³⁸ The situation in pure Ce is complicated at ambient pressure by the formation of a metastable dhcp β phase; this is conveniently avoided by studying Ce alloys containing small fractions of La and Th (see Ref. 23 and references therein).

³⁹ Similarly, no sharp feature in the differential susceptibility is seen in the case of the α to γ transition of Ce alloys²³; instead, the phase boundary is visible as a broad, rounded change in the gradient of $M(H)$ plots²³.

⁴⁰ H. Harima, private communication.

⁴¹ J. Singleton, Chapter 8 in *Band Theory and Electronic Properties of Solids* (Oxford University Press, Oxford, 2002).

⁴² As shown in Fig. 2(b), the upper boundary of the antiferromagnetic phase is mostly rather flat, varying by less than 0.35 K between 3 and 10 T. Our pulsed-field PDO measurements are constant-temperature field sweeps, so that they are rather insensitive to this part of the antiferromagnetic phase boundary; we observe merely some slight changes in shape of the $-\Delta f$ versus H curves in this region of field and temperature. The situation is further complicated by the fact that the PDO response is influenced both by changes in susceptibility *and* conductivity.

⁴³ P. Sengupta, C.D. Batista, R.D. Mc Donald, S. Cox, J. Singleton, L. Huang, T.P. Papageorgiou, O. Ignatchik, T. Hermannsdörfer, J.L. Manson, J.A. Schlueter, K.A. Funk and J. Wosnitza, *Phys. Rev. B* **79**, 060409 (2009).

⁴⁴ M. Kunz, W. Biberacher, N.D. Kushch, A. Miyazaki and M.V. Kartsovnik, preprint arXiv1696.07331 (2016).

⁴⁵ J. Singleton, *Rep. Prog. Phys.* **63**, 1111 (2000).

⁴⁶ We note that the terms “delocalized” (corresponding roughly to Cerium in the Ce⁴⁺ state) and “localized” (corresponding to Ce³⁺), though frequently used to describe such situations, represent at best a qualitative handwave that somewhat obscures the true quantum mechanics of the situation³¹.

⁴⁷ S. Imada, H. Higashimichi, A. Yamasaki, M. Yano, T. Muro, A. Sekiyama, S. Suga, H. Sugawara, D. Kikuchi, and H. Sato, *Phys. Rev. B* **76**, 153106 (2007).

⁴⁸ K. Hattori, Y. Hirayama, and K. Miyake, *J. Phys. Soc. Jpn.* **75** Suppl., 238 (2006).

⁴⁹ K. Hattori, Y. Hirayama, and K. Miyake, *J. Phys. Soc. Jpn.* **74**, 3306 (2005).

⁵⁰ T. Hotta, *J. Phys. Soc. Jpn.* **76**, 023705 (2007).

⁵¹ W. Y. Yuhasz, N. A. Frederick, P.-C. Ho, N. P. Butch, B. J. Taylor, T. A. Sayles, M. B. Maple, J. B. Betts, A. H. Lacerda, P. Rogl, and G. Giester, *Phys. Rev. B* **71**, 104402 (2005).

⁵² S. Sanada, Y. Aoki, H. Aoki, A. Tsuchiya, D. Kikuchi, H. Sugawara and H. Sato, *J. Phys. Soc. Jpn.* **74**, 246 (2005).

⁵³ T. Yanagisawa, W. M. Yuhasz, P.-C. Ho, M. B. Maple, H. Watanabe, T. Ueno, Y. Nemoto, and T. Goto, *J. M. M.* **310**, 223 (2007).

⁵⁴ T. Yanagisawa, W. M. Yuhasz, P.-C. Ho, M. B. Maple, H. Watanabe, Y. Yasumoto, Y. Nemoto, and T. Goto, *Physica B* **403**, 735 (2008).

⁵⁵ T. Yanagisawa, P.-C. Ho, W. M. Yuhasz, M. B. Maple, Y. Yasumoto, H. Watanabe, Y. Nemoto, and T. Goto, *JSPJ* **77**, 074607 (2008).